LA-UR-98-0112
Approved for public release; distribution is unlimited.

Title: **An intensified/shuttered cooled CCD camera for dynamic proton radiography**

Author(s): G. J. Yates, K. L. Albright, K. R. Alrick, R. A. Gallegos, J. Galyardt, N. T. Gray, G. E. Hogan, V. H. Holmes, S. A. Jaramillo, N. S. P. King, T. E. McDonald Jr., K. B. Morley, C. L. Morris, D. M. Numkena, P. D. Pazuchanics, C. M. Riedel, J. S. Sarracino, H-J. Ziock, and J. D. Zumbro

Submitted to:

An intensified/shuttered cooled CCD camera for dynamic proton radiography

G. J. Yates, K. L. Albright, K. R. Alrick, R. A. Gallegos, J. Galyardt, N. T. Gray, G. E. Hogan, V. H. Holmes, S. A. Jaramillo, N. S. P. King, T. E. McDonald Jr., K. B. Morley, C. L. Morris, D. M. Numkena, P. D. Pazuchanics, C. M. Riedel, J. S. Sarracino, H-J. Ziock, and J. D. Zumbro

Los Alamos National Laboratory, Los Alamos, NM 87545, USA

ABSTRACT

An intensified/shuttered cooled PC-based CCD camera system was designed and successfully fielded on proton radiography experiments at the Los Alamos National Laboratory LANSCE facility using 800-MeV protons. The four camera detector system used front-illuminated full-frame CCD arrays (two 1024 × 1024 pixels and two 512 × 512 pixels) fiber optically coupled to either 25-mm diameter planar diode or microchannel plate image intensifiers which provided optical shuttering for time resolved imaging of shock propagation in high explosives. The intensifiers also provided wavelength shifting and optical gain. Typical sequences consisted of four time phased images (1 microsecond spacing), one image from each camera. Each exposure was of about 500 ns duration and looked at a 40-ns proton burst on a fast scintillating fiber array. Camera design goals and measured performance characteristics including resolution, dynamic range, responsivity, system detection quantum efficiency, and signal-to-noise will be discussed.

KEYWORDS: high resolution, high speed, multi-frame, electro-optically shuttered, intensified, CCD camera system

1. BACKGROUND

A multiple frame imaging system has been designed for recording a variety of dynamic radiography experiments at Los Alamos National Laboratory (LANL) in support of the Department of Energy's Science Based Stockpile Stewardship (SBSS) program. The system records proton shadowgraph images of shock propagation properties of strategic materials in explosive environments. The time-dependent behavior of the shock front is recorded using a pulsed proton beam from LANL's 800-MeV linear accelerator at the Los Alamos Neutron Scattering Center (LANSCE). Visible images are generated by placing a scintillating fiber optic array in the beam path downstream of the material under test. The proton beam pulse structure consists of a 40-ns duration burst, with the bursts repeated at programmable intervals of 358 ns. Experiments described in this paper were taken with burst intervals of 1.074 μs.

The basic camera system combines a cooled slow scan CCD camera coupled to a gated image intensifier for shuttering. Electronic shuttering and/or interframe time of the CCD is too slow to adequately follow the repetitive proton generated images. Therefore, based upon our earlier works[1,2] electro-optic shuttering of microchannel plate image intensifiers (MCPIIs) by gating their photocathode emission was used. The intensifiers also provided gain for these weak photon flux experiments and provided wavelength shifting between input and output images for optimum spectral matching to the CCD. We refer to this camera configuration as an Intensified Shuttered CCD (ISCCD). The basic single frame camera concept is shown in Fig. 1. For

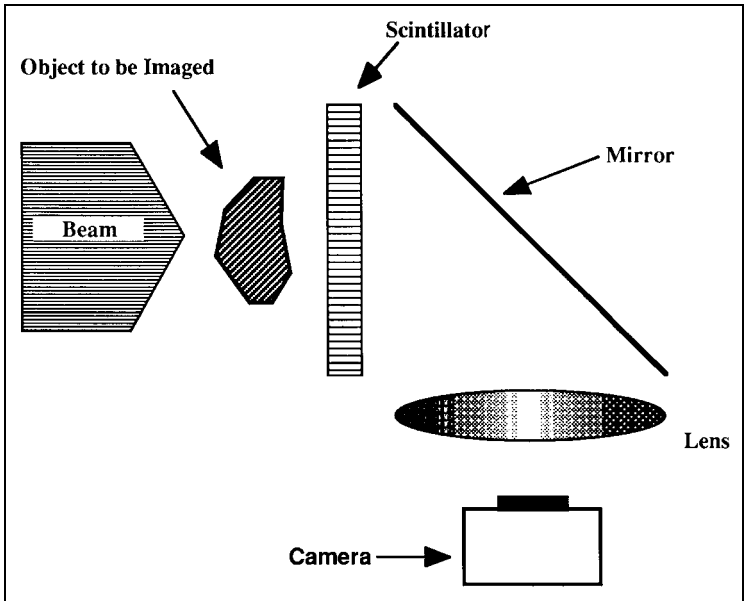

Fig. 1. Schematic of shadow-graph type imaging system.

dynamic radiography several such cameras are time-phased to record temporal and spatial evolution of shock wave fronts.

2. CAMERA SYSTEM COMPONENTS

The cooled CCD camera is manufactured by Pixel Vision Inc. of Oregon and utilizes front-illuminated Full Frame SITe CCD arrays of either 512^2 or 1024^2 24-micron square pixels. The camera is interfaced to a Dell Pentium desktop computer via a PCI BUS. The image intensifiers are 25-mm diameter proximity-focused planar diodes (PFD) or generation II MCPIIs. The 512^2 CCD cameras were fiber coupled (with Incom or Schott 25-17.4 mm tapers) to MCPIIs manufactured by DEP Inc., whereas the 1024^2 CCD cameras were fiber coupled (with Incom or Schott 25-mm plugs) to PFDs or MCPIIs manufactured by Proxitronic Inc. The higher spatial resolution PFD was used with the larger CCD to produce our highest resolution system.

The Pixel Vision 1024^2 SVXB10KS camera was directly compatible with earlier cooled/intensified/ shuttered CCD camera designs implemented at LANL, using their 512^2 SVXB512S camera. In particular, the SVXB10KS camera head could be used with LANL existing intensifier/vacuum-hermetic designs for the SVXB512S without any modifications.

The two image intensifier manufacturers, DEP Inc. and Proxitronic Inc., provided Super S-20 photocathodes, which have high quantum efficiency (QE) in the blue region of the visible spectrum. These photocathodes have peak sensitivity near 420 nm range, which matches the peak emission wavelengths of the scintillating fiber array used in the radiography experiments.

The DEP MCPIIs have quartz input faceplates and photocathodes with an electrically conductive under-coating to allow shuttering in the 5–50-ns range. This reduces their basic QE by approximately 30–50%, depending upon the light transmission of the undercoat. The Proxitronic intensifiers also had quartz input faceplates, but their photocathodes were not undercoated, thereby avoiding a reduction in their basic QE. Even without the undercoating, their photocathode conductivity remained sufficiently high to allow shuttering in the ≥350-ns range.

Because of the broad requirements for imaging camera performance, such as wide dynamic range, variable gain, signal-to-noise, and tradeoffs between gain and resolution requirements, we decided to use both DEP MCPII and Proxitronic PFD intensifiers, to exploit the best features of each type. The MCPIIs have higher gain and faster shuttering with lower high voltage and gate pulse amplitude requirements. The PFDs have higher QE, higher resolution and lower noise, but require much higher bias and gate potentials. Both have adequate dynamic range to effectively use the SITe CCD pixel well capacity. We are still evaluating tradeoffs between the two intensifier types. The salient characteristics of the CCD camera and image intensifiers are given in Table 1.

Table 1. Salient characteristics of the CCD cameras and image intensifiers.

Pixel Vision CCD Camera Specifications		
CCD camera	SVXB512S	SVXB10KS
Image Sensor	SITe SI502AB	SITe SI003AB
Image Region	12.3 mm × 12.3 mm	24.6 mm × 24.6 mm
Active Pixels	512 (h) × 512 (v)	1024 (h) × 1024 (v)
Pixel Pitch	24 ¨µm (h) × 24 µm (v)	24 µm (h) × 24 µm (v)
Full Well Capacity	> 350,000 electrons	> 350,000 electrons
DEP PP0340AE Microchannel Plate Intensifier Specifications		
Wavelength	400 nm	440 nm
Spectral Sensitivity	50.2 mA/W	72.0 mA/W
Quantum Efficiency	~16%	~20%
Luminous Gain	2000–5000	
Spatial Resolution	32 λp/mm	
Shutter Speed	< 50 ns	
Proxitronic BV 2502QZ10 Planar Diode Intensifier Specifications		
Wavelength	400 nm	440 nm
Spectral Sensitivity	78.30 mA/W	73.08 mA/W
Quantum Efficiency	~24%	~21%
Luminous Gain	3–10	
Spatial Resolution	58 λp/mm	
Shutter Speed	< 500 ns	

The cooled CCD camera design requires operation in either a vacuum or dry gas environment to avoid condensation at temperatures colder than ambient. LANL designed the vacuum-hermetic seal housing for coupling the intensifiers to the CCD. The mechanical design shown in Fig. 2 was used for coupling a 25-mm MCPII to the 12.3-mm square image area for the 512^2 pixel CCD. This required the use of reducing fiber optic couplers with demagnifications of either 2.03:1 (25 mm to 12.3 mm) for mapping the full CCD area onto the MCPII, or 2:1.44 (25 mm to 17.4 mm) for mapping the full MCPII area onto the CCD. A similar design was used for coupling the 25-mm PFD to the 24.6-mm square 1024^2 CCD, but with non-reducing fiber-optic plugs. The outer diameters and

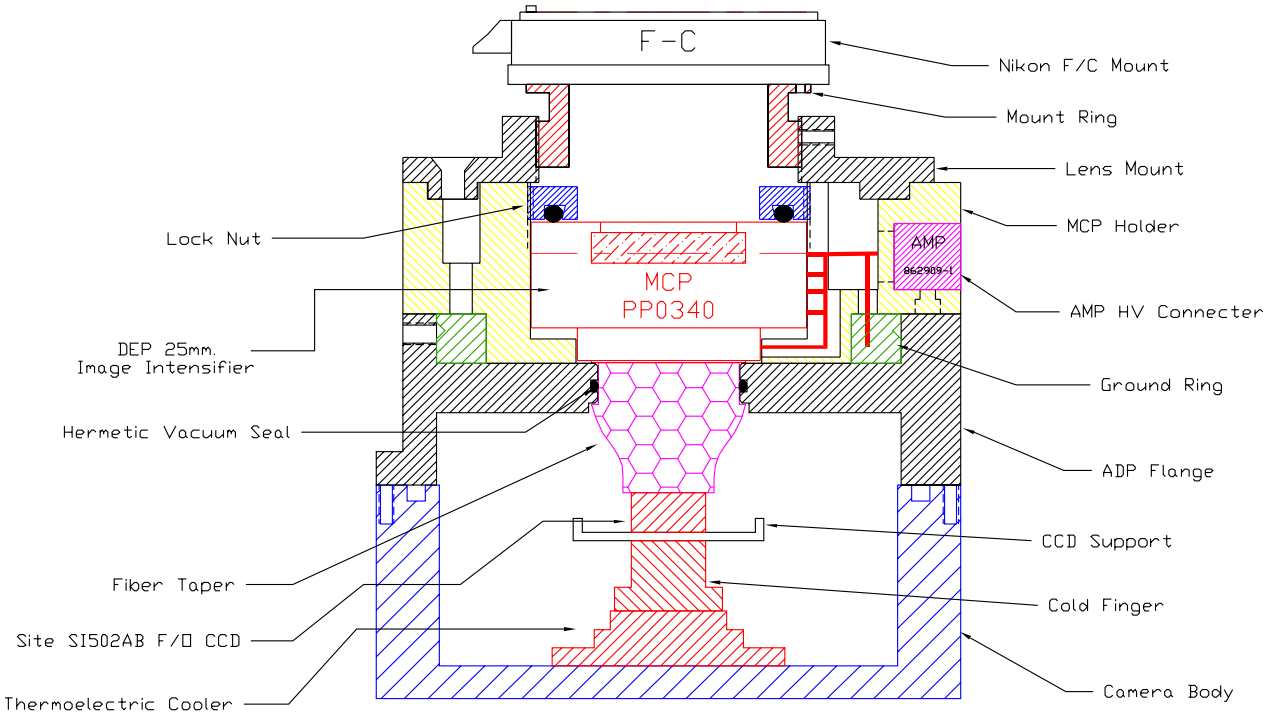

Fig. 2. Camera head section illustrating the vacuum-hermetic seal design (lower part of drawing), the intensifier housing assembly (mid portion), and lens mount (upper portion). The F/O faceplate is bonded to the CCD.

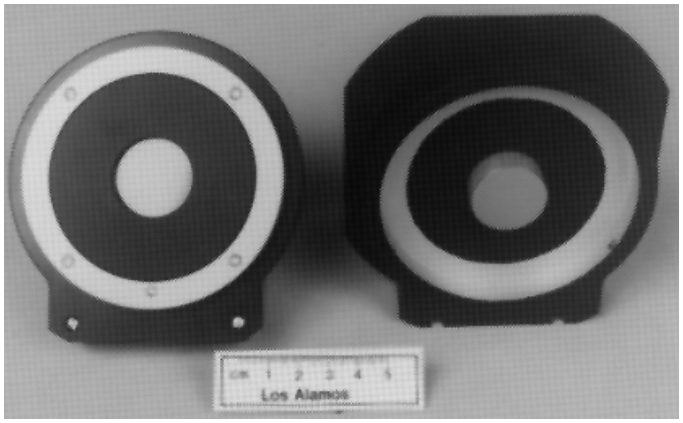

Fig. 3. Photograph of the intensifier housing assembly (left) with the DEP MCPII, and the vacuum-hermetic seal assembly (right) and its fiber optic coupler.
to allow utilization of the same vacuum-hermetic seal design.

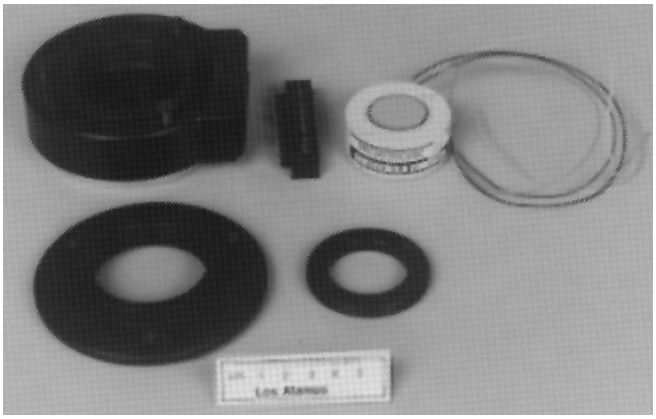

Fig. 4. Photograph of the intensifier housing assembly components including the Proxitronic PFD (top right).
overall lengths of all the fiber-optic couplers were identical

Figures 3 and 4 are photographs of the MCPII and PFD housings and components. Figure 5 shows the coupled MCPII/CCD camera head with optical lens, intensifier housing, vacuum dewar, and LANL MCPII control package. The complete camera, except for the computer, is shown in Fig. 6.

The Pixel Vision cameras are personal computer (PC) controlled, and use a 16-bit digital input interface to PCI, ISA, or PCMCIA buses. We used a Dell Pentium 233-MHz PC with 60 megabytes of memory, a Windows 95 operating system, and a PCI bus which had serial fiber-optic transmitter/receiver links to allow remote control and data acquisition of the cameras at distances of approximately 220 ft.

The camera has control, calibration, graphics, and analysis software. Controls include pixel binning, region-of-interest (ROI) for image area truncation, readout rate, amplifier gain, and integration or exposure interval. Calibration controls include two-

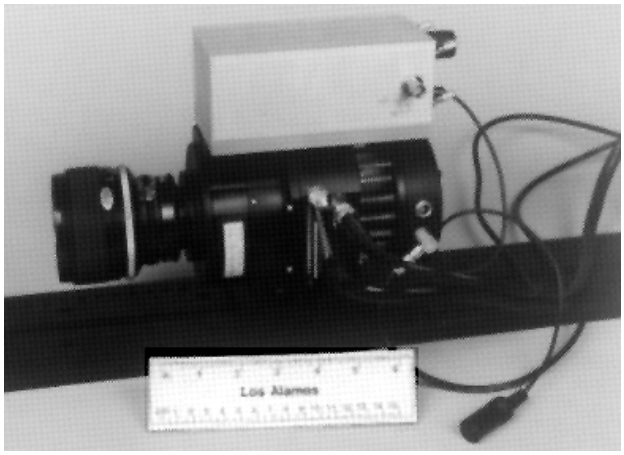

Fig. 5. The ISCCD camera head. The MCPII gate width and gain controls are in the RF box on top of the camera.

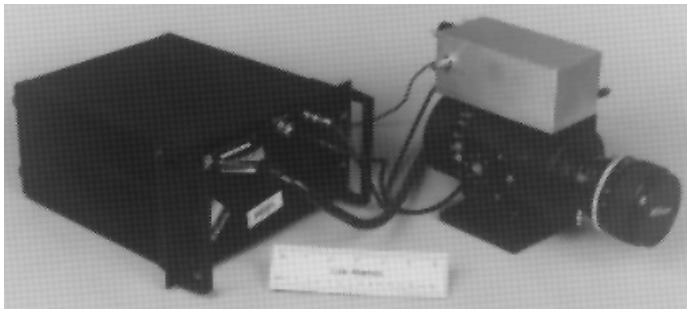

Fig. 6. The complete ISCCD camera showing the Pixel Vision control unit (left) and the head (right) with LANL MCPII/PFD components (right).

point corrections for dark current and QE variances from pixel to pixel in the arrays. Analysis software includes derivation of statistical variables such as mean, variance, standard deviation, minima, and maxima of stored images.

3. CAMERA CALIBRATIONS

(a) Integration Periods

The ISCCD integration linearity for the few-second range exposures, with the MCPII operated in its DC or non-gated mode, while being exposed to a DC light source was measured. One of the 512^2 cameras was used for these tests. A small, low intensity, circular spot of light was imaged onto the MCPII photocathode and the CCD camera was operated in its "internal" exposure mode with the integration periods selected by software. Integration periods of 2, 4, and 8 seconds were used. Figure 7 shows data for one exposure. The fluctuations in the dark, baseline region reflect the electronic noise in the camera, while the larger fluctuations in the light spot region are due to counting statistics and the resulting variable gain in MCPIIs found at low illumination levels[2]. Amplitudes were calculated by measuring the peak values above baseline, using the average amplitudes at peak and base as references. This gave approximately 276, 562, and 1102 amplitude digital units (ADUs), respectively, for the 2-, 4-, and 8-second integrations, which is within a few percent of expected values, and is well within experimental accuracy of the measurements. These tests were performed to look at dark current buildup effects with time. To a first approximation, none were noted, attesting to the effectiveness of the peltier cooling. The tests were done at 246° K.

(b) Gated Performance

These tests examined the MCPII gate transmission vs. gate duration in the 200 ns to 2 μs range. The CCD camera was operated in "external" exposure mode where it was commanded to go into its integrate mode 60 μs prior to strobing light onto the MCPII photocathode. The MCPII shutter gate is time-phased to be coincident with the peak emission of a xenon flash of ≈ 3 μs FWHM. The gate width was varied and the resulting CCD video amplitude was recorded. The waveforms of Fig. 8 illustrate the time-phasing among the strobe light, MCPII shutter, and CCD exposure period.

Values of 11,000, 21,312, 38,543, and 48,621 ADUs were obtained for 200 ns, 400 ns, 800 ns, and 1.6 μs MCPII gates, respectively, for one 1024^2 camera (ISCCD#1). The data track the gate widths less well for longer gates due to the falloff of light output by the xenon flash at later times. Similar data for a second 1024^2 (ISCCD#2) camera gave 11,942 and 22,376 ADUs for 200-ns and 400-ns MCPII gates. These data are useful to indicate that the MCPII gates transmit approximately linearly with duration. (A light source with a flatter broader peak would have given better results.)

(c) Dynamic Range

The 1024^2 ISCCD#2 was operated with the MCPII in the gated mode and the CCD in its external exposure mode. The xenon pulsed light source was time phased with the MCPII shutter and CCD integrate cycles as shown earlier in Fig. 8. A 400-ns MCPII gate was centered on the 3-μs strobe pulse and neutral density (ND) filters were used to attenuate the light to

generate the transfer curve. The MCPII gain operated near mid-range. A blue narrow-band transmission filter was used to provide 415 ± 20 nm illumination. A nominally 1 cm^2 aperture at the light source was imaged onto the MCPII photocathode.

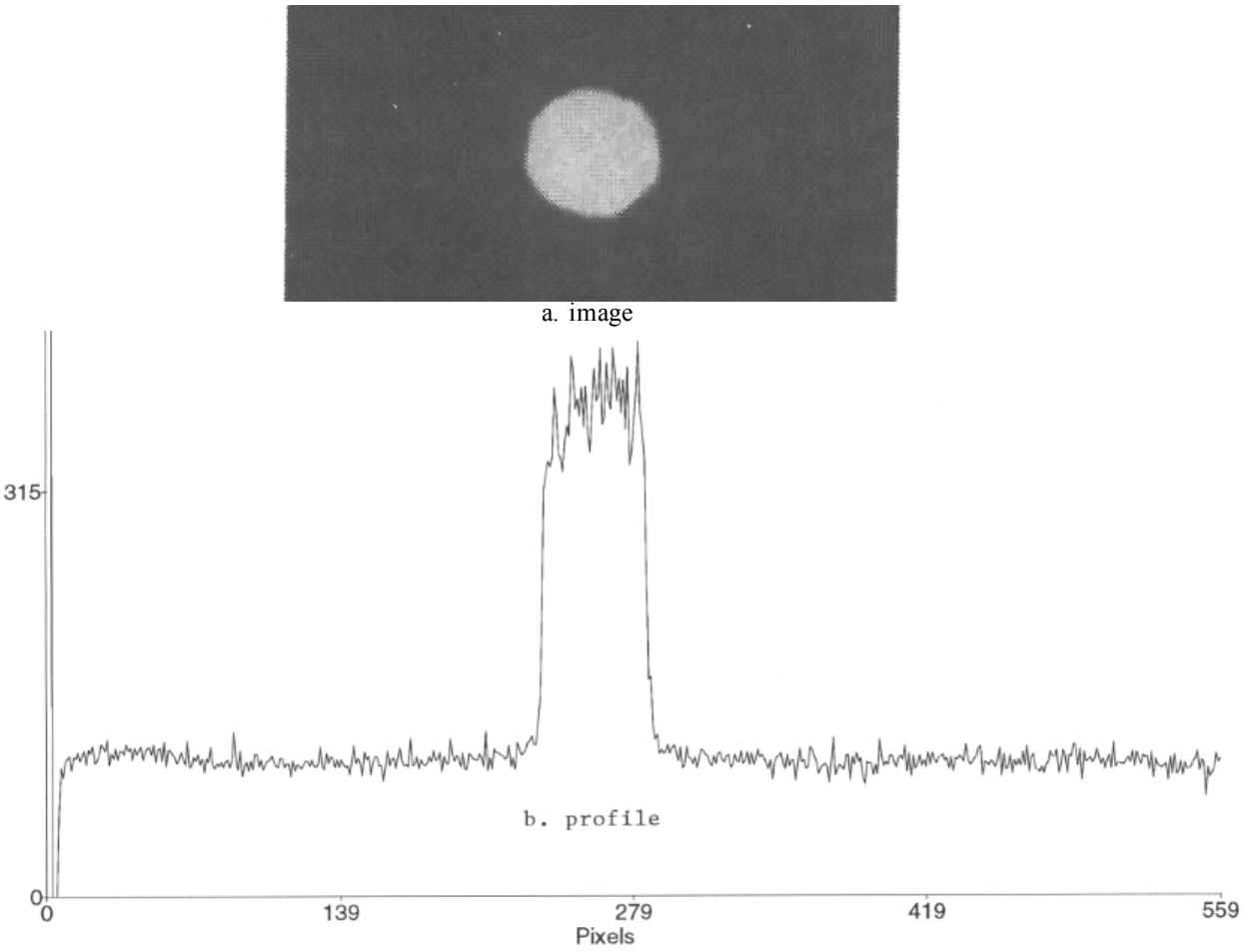

Fig. 7. Image of the light spot (a) and the signal amplitude (b) obtained from CCD integration time of two seconds with continuous light illumination using a 512^2 CCD coupled to the MCPII. The vertical scale is in ADUs.

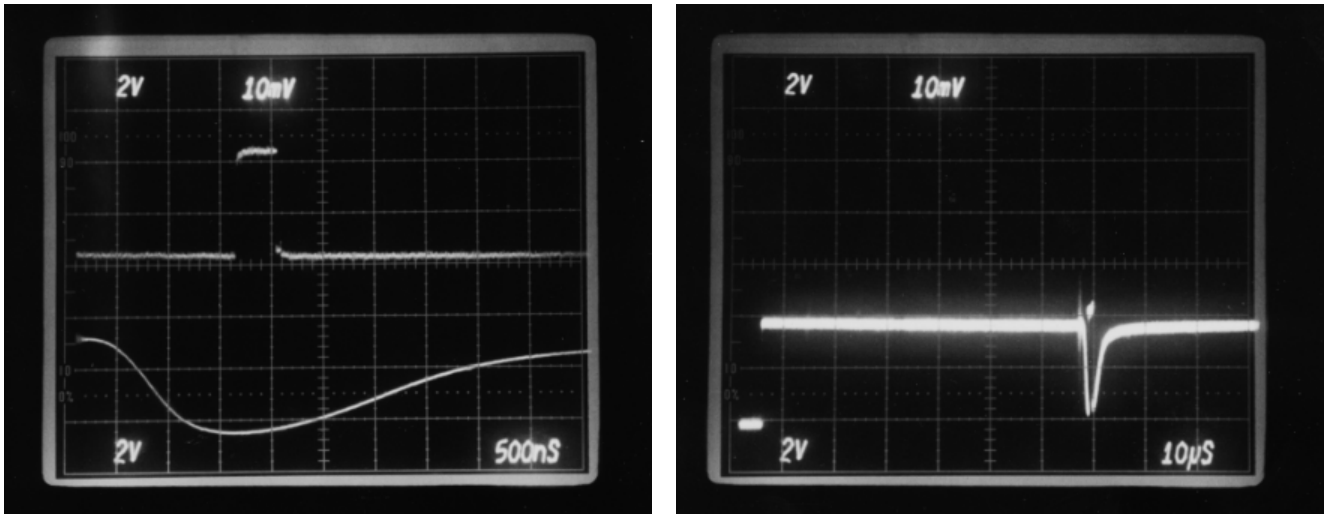

Fig. 8. The left-hand photograph shows the MCPII 400-ns gate pulse (top) and Xenon strobe light pulse (bottom). The right-hand photograph shows the "added" waveforms corresponding to CCD camera exposure/integrate interval and the gate and light pulses ≈ 60 μs into exposure interval..

The results of the measurements are given in Table 2. For each neutral density filter value the average ADC counts/pixel in the area of the light spot (SPOT column) and in a corresponding area outside of the light spot (DARK column) were recorded. The difference of these values are given in the SPOT - DARK column, which were then plotted as a function of neutral density filter value in Fig. 9. Also shown in that figure are the results from a second ISCCD camera. Table 2 also gives the fractional standard deviation (S.D.) values associated with the pixel values in the PEAK and DARK areas. The standard deviation values are indicative of the photoelectron counting statistics and sources of noise in the ISCCD system.

(d) Lens Transmission versus Wavelength

The percent transmission of several optical lenses was measured at several wavelengths covering the range of candidate scintillator emission spectra. The two principal candidate scintillators were NaI(Tl), which peaks at 415 nm, and BCF-99-55 scintillating fiber array[3] with peak emission at 432 nm. Figure 10 shows the transmission factors observed. The data were taken using an optical spectrometer (Optronic model 740) as the source and a photodiode (Optronic 730A) for the detector.

(e) Resolution

The ISCCD system resolution was measured with the same setup used for the dynamic range measurements described earlier, but a calibrated transparent resolution pattern, $\approx (2.75 \text{ in})^2$, replaced the $\approx 1 \text{ cm}^2$ aperture at the strobe. The pattern has five bar sets (each consists of three opaque and two transparent bars of equal width). The resolution image for a 1024^2 CCD (ISCCD#2) coupled to a 25-mm Proxitronic MCPII is shown in Fig. 11. The spatial frequencies increase from the right edge-to-center and from the bottom-to-center. At the strobe plane, the first set is 1 λp/mm, the second is 1.4 λp/mm, the third is 2.0 λp/mm, the fourth is 2.85 λp/mm, and the fifth is 4 λp/mm. Similarly, from the left edge-to-center and from the top-to-center, spatial frequencies increase as follows: the first set is 0.86 λp/mm, the second is 1.22 λp/mm, the third is 1.71 λp/mm, the fourth is 2.44 λp/mm, and the fifth is 3.43 λp/mm.

The demagnification from the strobe plane to the MCPII plane was ≈ 0.17, which increases the above frequencies by a factor of 5.87. Column and row profiles from Fig. 11 indicate approximately equal resolution in both horizontal and vertical axes as expected. The apparent limiting resolutions are in good agreement with the Nyquist limit of 20.8 λp/mm expected from the pitch of the 24-micron CCD pixels. The apparent resolution beyond the

Table 2. Dynamic range measurements for ISCCD#2 in ADU's. Fractional standard deviation (S.D.) values are also given.

ND Filter	Spot	Dark	Spot - Dark	Spot S.D.	Dark S.D.
0.0	41,616	3,215	38,401	0.0176	0.0082
0.3	27,656	3,090	24,566	0.0393	0.0072
0.6	14,465	2,994	11,471	0.0357	0.0072
1.0	7,031	2,935	4,096	0.0495	0.0175
2.0	3,447	2,915	532	0.0187	0.0028
3.0	2,933	2,910	23	0.0071	0.0030

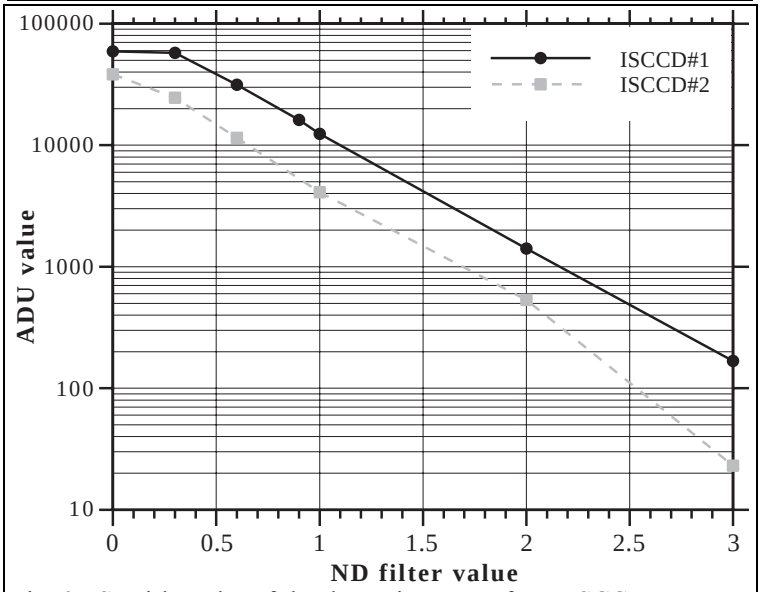

Fig. 9. Semi-log plot of the dynamic range of two ISCCD cameras. As is evident from the figure, the gains of the two cameras were not set to be identical, and ISCCD#1 began to saturate at the highest light intensity.

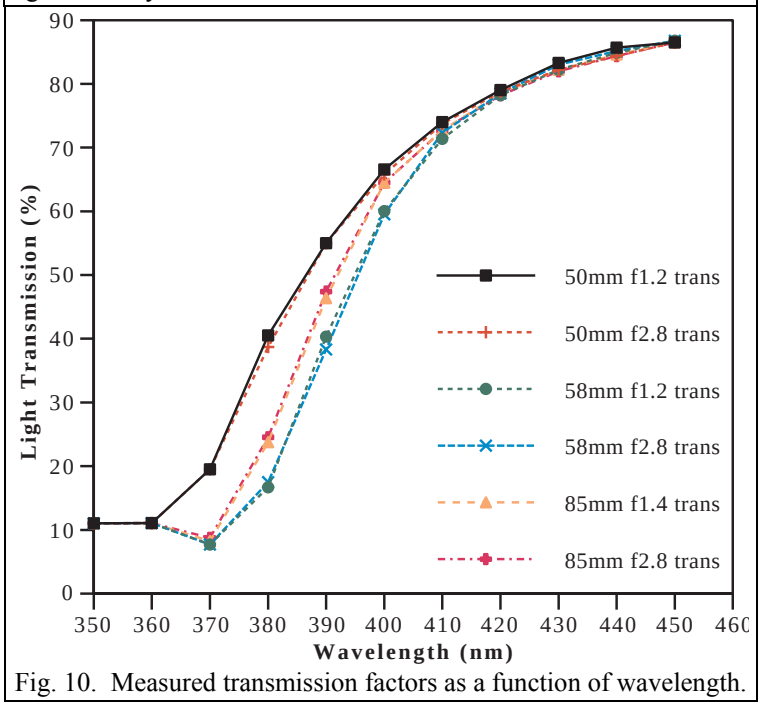

Fig. 10. Measured transmission factors as a function of wavelength.

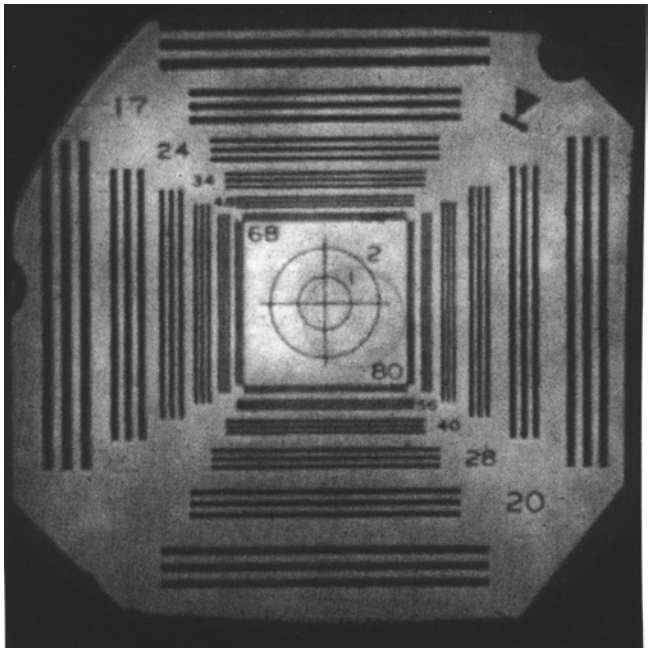

Fig. 11. Image of resolution pattern from one of the 1024^2 CCDs coupled to a 25 mm MCPII, gated for 400 ns and illuminated with the strobe pulsed light source. The shading in the image is due to non-uniform illumination.

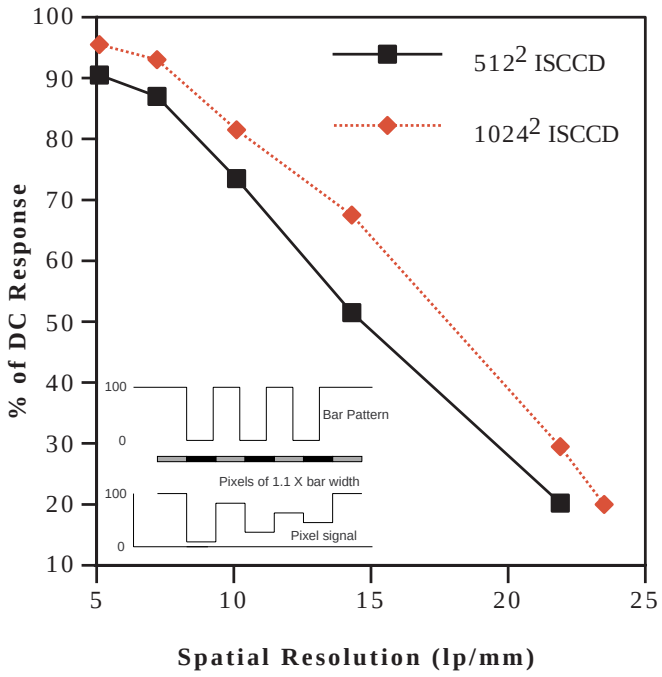

Fig. 12. MTF measurements for 512^2 and 1024^2 CCDs coupled to MCPIIs.

Nyquist limit is an artifact. For a limited number of bars and proper alignment with the pixels, modulation of the CCD signal can still be achieved as shown in the Fig. 12 inset.

The modulation transfer function (MTF) for the spatial frequencies in this image are plotted in Fig. 12. Similar MTF data from a 512^2 CCD coupled to a 25-mm DEP MCPII are included. The 1024^2 unit shows the best MTF. The 512^2 resolution is the poorer, primarily due to the demagnification between the MCPII and CCD. More detailed analysis of other intensifier/CCD combinations are in progress.

4. PROTON RADIOGRAPHY EXPERIMENT

The detector system described above was used in an experiment that studied the propagation of detonation waves in high explosives. The experiment relied on a new diagnostic capability developed at Los Alamos National Laboratory, in which radiography is carried out using protons as the probing particles. For applications, in particular those involving rapidly cycled multiple exposures, thick objects, and/or material identification, proton radiography has many advantages over X-ray radiography. For instance, in proton radiography the probing particles are the primary beam particles, are nearly mono-energetic, and can be detected with essentially 100% efficiency, even by thin detectors. Proton accelerators also naturally produce a strobed multiple pulse beam ideal for studying dynamic events and freezing motion. Protons interact both via the nuclear force and the Coulomb force, which have different dependencies on material type. Because of this, material identification can be done easily using protons. Another advantage of protons is their large nuclear interaction/scattering/attenuation length, which makes them well suited for radiographing thick objects (hundreds of g/cm^2 of material) and for keeping scattered backgrounds at very low levels. In addition to the nuclear out-scattering, the protons, being charged particles, undergo Multiple Coulomb Scattering (MCS) to small angles by the object. Unless that is corrected for, a blurred image results. However, the charge of the protons also allows them to be steered by magnetic fields. In particular, an imaging magnetic lens can be made which focuses the scattered protons to form an image of the object. The magnetic lens we used[4] consisted of a set of four quadrupole magnets arranged as two pairs of doublets. Such a lens, as illustrated in Fig. 13, not only forms an image of the protons scattered to small angles by MCS, but at its midpoint sorts all protons radially by scattering angle, regardless of what part of the object they passed through. At the midpoint of the lens a radial aperture can be inserted to produce a cut on the object caused angular scattering of the beam. That cut can be tuned to provide maximum contrast of the resulting image yielding maximum information content. This can also be done for very thin objects for which there is virtually no nuclear attenuation of the proton beam. In that case, the attenuation is effectively

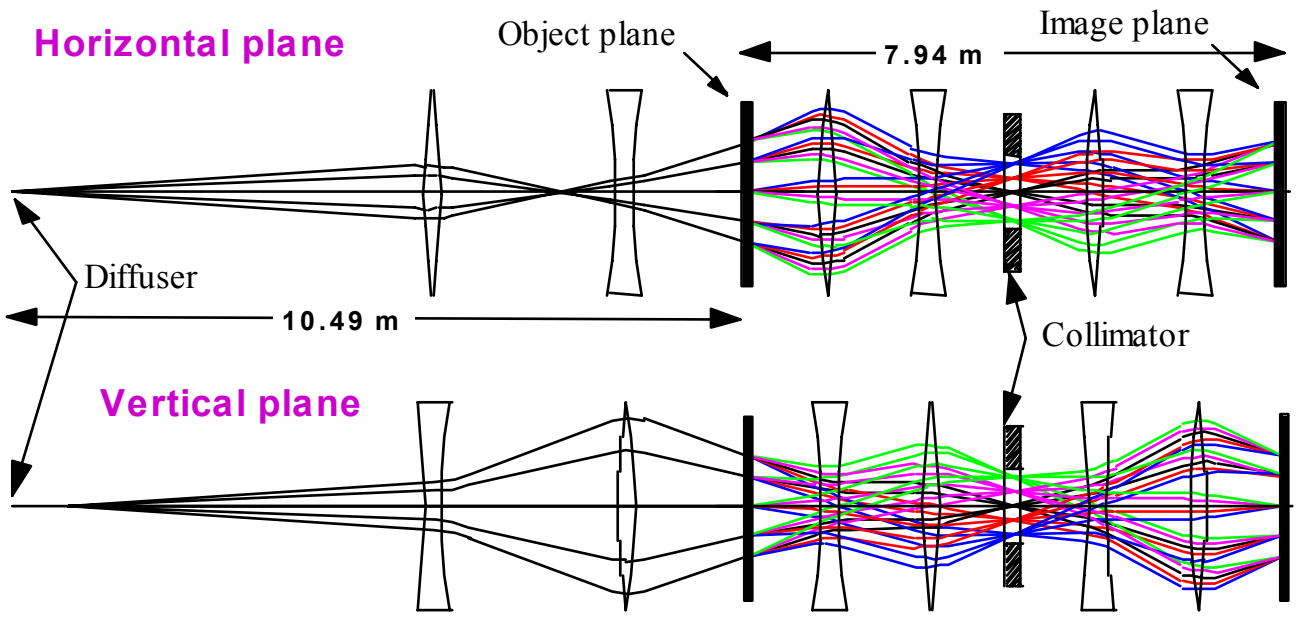

Fig. 13. X- and Y- plane ray traces for the magnetic lens system used in the experiment. The incident proton beam was expanded with a diffuser and an upstream lens set, which also established a correlation between particle location and angle at the object plane. The correlation reduced aberrations in the subsequent inverting identity lens. The identity lens consisted of four quadrupole magnets. Multiple Coulomb scattering of the proton beam by the object is schematically indicated. Scattered rays are at angles of ±10, ±5, and 0 mrad with respect to a "nominal" ray. The radial angle sorting at the midplane of the lens (collimator location) is clearly evident. (The transverse scale is greatly expanded relative to the longitudinal scale.)

caused by the Coulomb interaction as opposed to the nuclear interaction. Furthermore, by stacking two such identical lens systems back to back, the only difference being a smaller angular aperture in the second lens, one can do material identification.

For the experiment, we made use of the chopped beam at LANSCE. The LANSCE accelerator, whose time structure is given in Fig. 14, is an 800-MeV linac, which operates at a fundamental frequency of 201.25 MHz. As such, one micropulse of protons (200 ps width) comes once every ~ 5 ns. In the chopped mode of operation used for our experiment, the beam is gated on only once every 72 micropulses or every ~ 358 ns. Depending on the duration of the gate, one such chopped burst can contain several micropulses. We typically used ~ 40 ns of beam for a burst. The chopped beam can be further gated so that only one in every N chopped bursts actually contains beam. For our experiment we had $N = 3$, or one ~40 ns burst of protons every 1.074 μs Thus the electro-optical shutters for our cameras (the MCPIIs and PFDs) could be operated relatively slowly. The only requirement was that they go from totally opaque to totally transmissive and back in a period of 1074 ns, and that they maintain the totally transmissive point for at least the full 40 ns period when the beam was actually present.

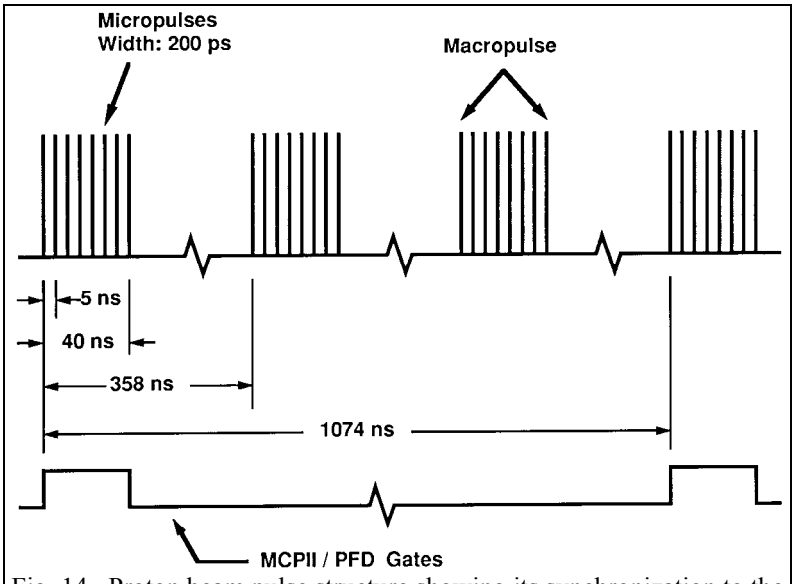

Fig. 14. Proton beam pulse structure showing its synchronization to the MCPII/PFD shutter gate.

The object we radiographed for the following discussion was a hemispherical piece of high explosive, ~ 57 mm in diameter, with a mean density of ~1.9 g/cc. A calculation of the spatial resolution of the magnetic lens system used gives a value of approximately 1/4 mm. A static radiograph of the explosive charge is shown on

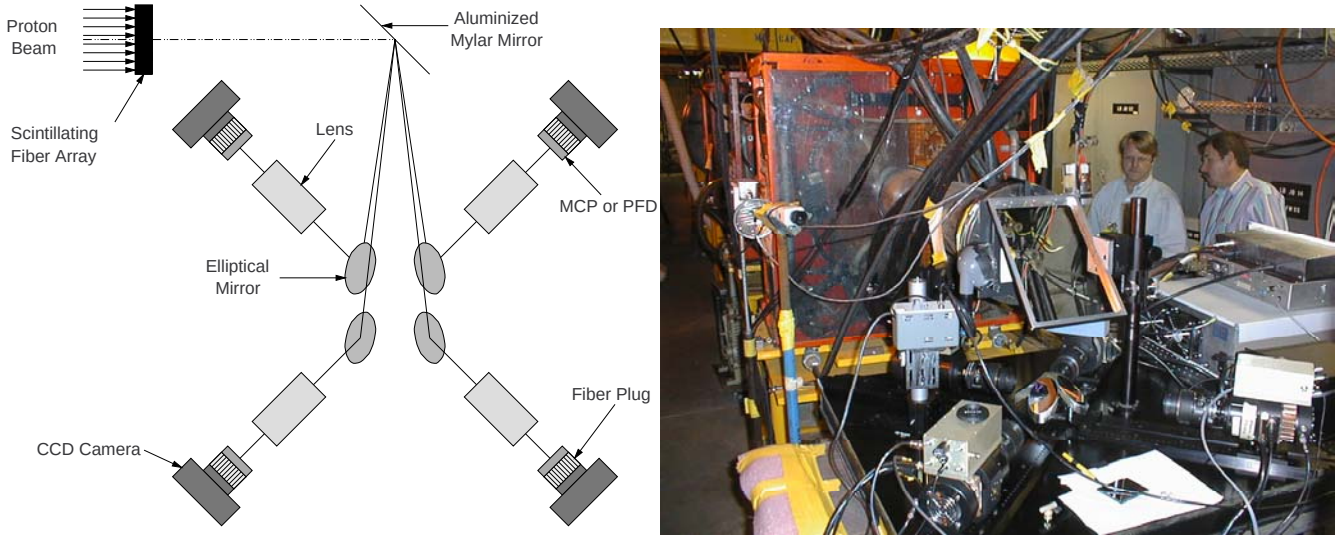

Fig. 15. Schematic of the detector system used in the radiography experiment is shown on the left, and the corresponding photograph is shown on the right. The cameras and lenses were in a common horizontal plane which was below the proton beam. In the photograph, the proton beam was coming out of the page.

the left side in Fig. 16. The detonator is centrally located at the bottom of the explosive charge and is clearly visible in the "hole" with two wires coming out.

The layout of the experimental setup is shown in Fig. 15. The light from the scintillating fiber array was directed downward out of the plane of the proton beam by the aluminized mylar mirror. From there it was directed by elliptical mirrors back into a horizontal plane in which the four ISCCDs and their lenses were located. The different cameras were gated on sequentially so that each camera saw a different beam burst. The images recorded by each of the three working cameras are "shown" in Fig. 16. In reality what is shown are various ratios of images. The left column shows the ratio of a radiograph of the static object to a "radiograph" of the beam profile. The central column is the ratio of dynamic object radiograph to the "radiograph" of the beam profile. Finally, the right column is the ratio of the dynamic object radiograph to the static object radiograph. The use of dynamic to static ratios brings out the differences between the static and dynamic radiographs. Ideally properly beam normalized ratios of identical images would yield a uniformly gray image with the object being invisible. A slight movement of the object between two exposures would produce a ratioed image in which all the edges and discontinuities in the object stand out. This is the explanation of the ghostly outline of the object seen in the right hand column in Fig. 16. In addition to the outline seen in the right column, a growing hemispherical region is clearly evident inside the explosive. The boundary of the hemispherical region is the shock front of the exploding material. This region is compressed and thus has higher density and therefore more strongly attenuates the proton beam than the same region in the static radiograph. This results in a ratio which is less than one, and thus appears as a dark region in the ratio image. As one moves down the column to later times, the diameter of the shock front has clearly grown, almost reaching the physical boundary of the explosive in the lowest row. The rarefaction that occurs behind the shock is visible as the lighter to white region. Below that one can also note the compression in the material on which the explosive was resting. The high velocity of the shock wave relative to the mechanical motions induced by the explosion is evident as the explosive itself and the stand it was resting appear to have hardy moved between exposures. Close examination of the late images does however show some minor motion of the bulk material as is evidenced by the thin dark and light horizontal bands at the interface between the stand and the high explosive.

For the images shown, the camera systems were operated with the optical lens system set to yield a magnification of ~1/5 so that each 24 μm pixel of the CCD corresponded to 120 μm at the object plane for the 1024^2 pixel CCDs. (The magnetic lens operated at unit magnification). The beam fluence put through each such unit area at the center of the object was ~10,000. The incident beam profile had a Gaussian profile with a sigma at the object of 3.4 cm.

An examination of the counting statistics for a single pixel in the 1024^2 pixel CCD cameras reveals that even though a 2.5 cm piece of scintillator was used, slightly less than 1 photoelectron per proton was the best that was achieved at the photocathode of the intensifier in the camera system. This number is indicative of the problems of using lens coupled

systems, especially when a small image size (magnification) is required, which in our case is dictated by the intensifier photocathode size (25 mm). The fraction of forward light (0° to 180°) accepted by a lens system from a point source is

$$fraction = 1 - \cos\{\text{atan}[M/(2F(1 + M))]\} \quad (1)$$

where F is the f# of the lens, and M is the magnification the lens system. For small values for the argument of the arctangent, the above expression can be approximated by

$$fraction = (M^2) / [8F^2(1 + M)^2] \quad (2)$$

Putting in values representative of those we used (M = 1/5, F = 2.8) gives $fract = 4.4 \times 10^{-4}$. This value is then effectively further reduced by a number of other factors. These include the fact that the scintillator is itself a fairly high index material

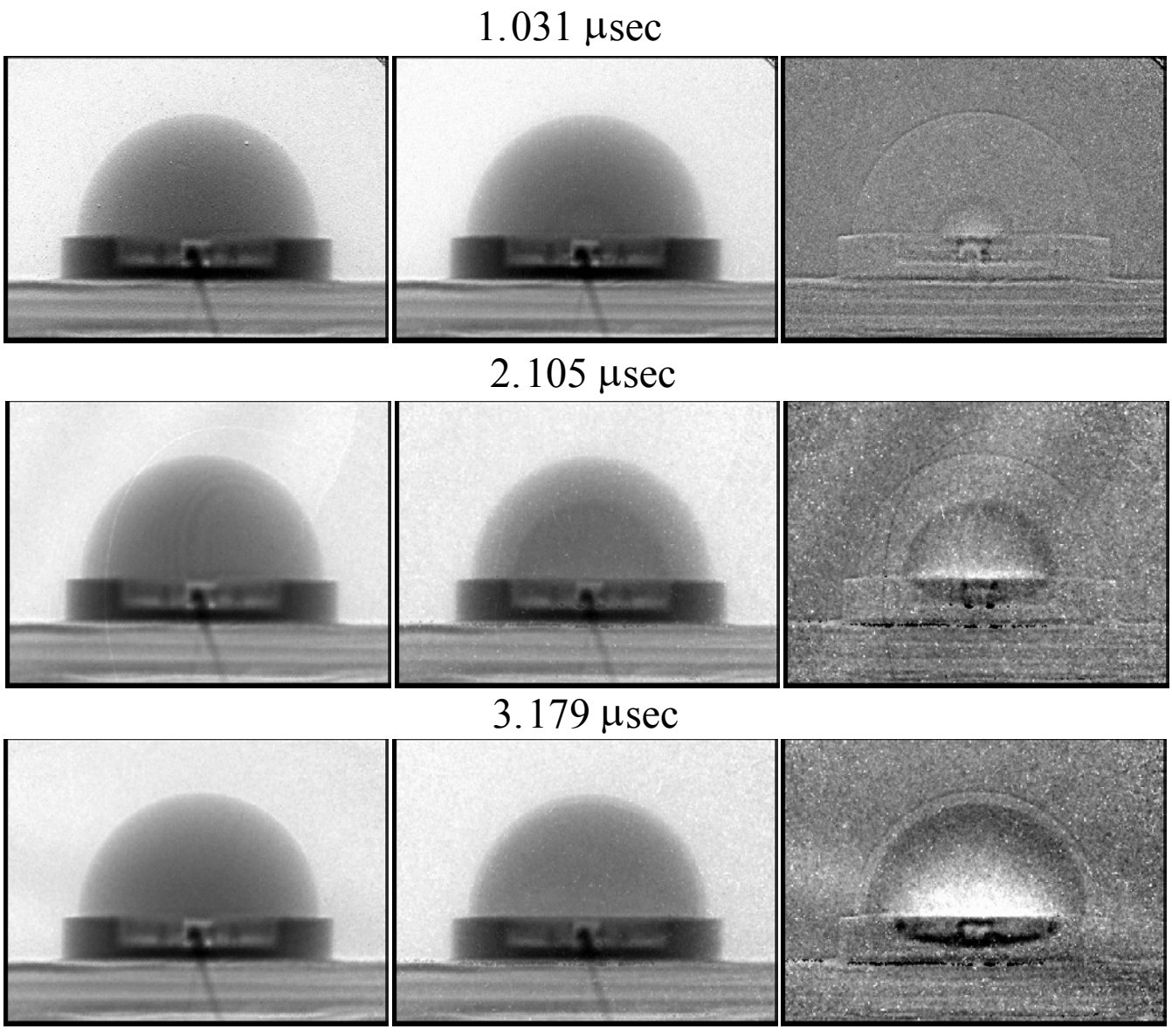

Fig. 16. Ratio images of proton radiographs taken by the detector system. Each row corresponds to a different ISCCD. The fourth ISCCD was unfortunately disabled by a lightning strike shortly before these radiographs were taken. The three different columns correspond to beam normalized radiographs of the static object (left column), beam normalized radiographs of the object as it was exploding (center column), and ratios of the dynamic to static images (right column), which emphasize differences between the static and dynamic radiographs. The given times are relative to detonator breakout.

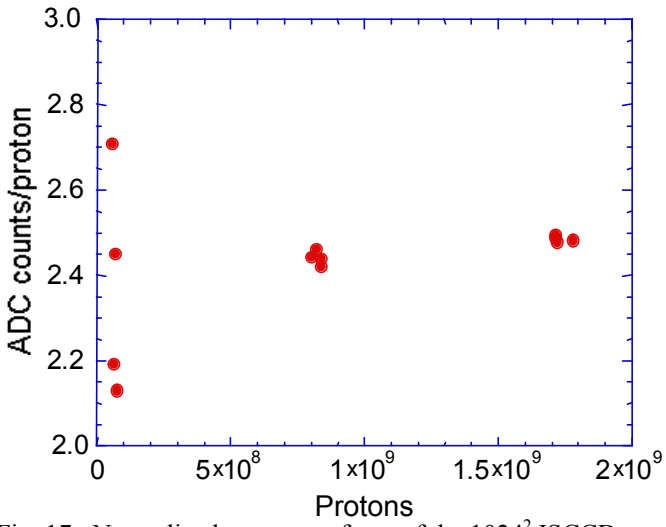

Fig. 17. Normalized response of one of the 1024^2 ISCCDs as a function of proton beam dose. At each of the three beam nominal intensities, four measurements were made.

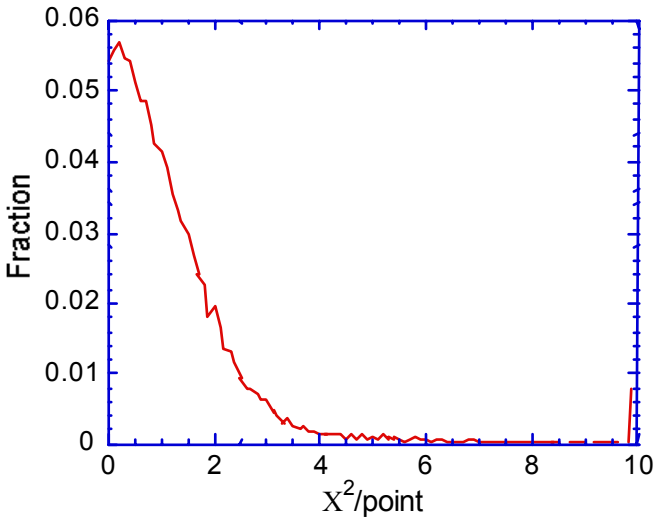

Fig. 18. Histogram of the individual values for the argument of the sum in Eq. (4).

(n = 1.6) and the light is refracted to larger angles on leaving the scintillator, or equivalently, compressed to smaller angles when projecting back from the lens into the scintillator. There is also a packing fraction associated with the scintillating fiber array and the light transmission of the optical system is not 100%, especially for the blue light emitted by the scintillator. The largest factor is however the quantum efficiency of the photocathode of the gated intensifier, which is about 20%. When all these inefficiency factors are taken together, they reduce the overall efficiency of the system at least another factor of 20. To set the scale, an 800 MeV proton typically produces on the order of 15,000 "forward" photons in a 1 cm thick plastic scintillator, if one mirrors the backside of the scintillator. Thus a 2.5 cm piece of scintillator for the lens system parameters given above results in about 0.8 photoelectrons per proton.

To improve the performance of future camera systems we plan to improve the number of photoelectrons per proton by using larger diameter MCPIIs or PFDs (40 mm vs. 25 mm) throughout, which allows the system magnification to be increased from the value of 1/5 to 1/3, yielding a factor of 2.25 more light. At the same time we hope to use faster lenses to increase light collection efficiency.

5. CAMERA PERFORMANCE DURING THE EXPERIMENT

We have normalized a series of camera exposures at different proton doses with no object in the beam in order to measure the camera linearity. The proton dose was measured using a current transformer in an upstream location before any of the magnets. The transmission through the system, from the transformer to the radiation to light converter, has been assumed to be unity. The results are displayed in Fig. 17. Although these measurements were limited by the accuracy of the proton flux determination at the lowest fluxes, the reproducibility and linearity of the combined system can be seen to be on the order of 2% at doses up to 1.8×10^9.

In addition to the calibration, the pixel by pixel fluctuations between different exposures normalized to the proton flux have been used to determine the detection quantum efficiency (DQE) of the camera systems. The ratio of the measured fluctuation level was compared to that expected due to the proton counting statistics, and the ratio was used to extract the DQE. For a single element of a detector the DQE is defined as:

$$\mathrm{DQE} = \left(\frac{\sigma(n_e)}{n_e}\right)^2 \Big/ \frac{1}{n_p}, \qquad (3)$$

where $\sigma(n_e)$ is the *rms* fluctuation level in the measured signal, n_e, and $\sqrt{1/n_p}$ is the expected fluctuation level due to the quantum counting statistics in the incident number of primary particles, in this case protons. For a perfect detector the DQE is unity. We have extracted the DQE from our camera data by comparing images and averaging over pixels. We have filtered out pixels with very large fluctuations levels caused by nuclear interactions in the CCD. This amounts to less than

1% of the data typically. The individual images were normalized to the incident number of protons measured in the upstream transformer. The DQE was extracted using:

$$\frac{\sum_{i=1}^{pixels} \frac{(n1_i - n2_i)^2}{(n1_i + n2_i)}}{pixels} = \frac{1}{\mathrm{DQE}}. \quad (4)$$

Here, $n1_i$ and $n2_i$ are the signal levels normalized to number of protons, from two different images averaged over the pixels, i. The histogram of the individual values for the argument of the sum in Eq. (4) is shown in Fig. 18. We found that a typical value for the DQE for the 1024^2 camera with the PFD gate was about 0.60, and for a 512^2 channel MCPII gated ISCCD the detection quantum efficiency (DQE) was about 0.40. This compares favorably with the value of 0.44 gotten using a simple estimate based on eq. (5):

$$\mathrm{DQE} = 1 / [1 + (1 / n_{p.e.})], \quad (5)$$

where $n_{p.e.}$ is the number of photoelectrons per proton, which was estimated to be 0.8 in Section 4.

6. CONCLUSION

We have designed and constructed a 4 frame high resolution, high speed CCD camera system which was successfully fielded in dynamic proton radiography experiments at LANSCE. Images were recorded with interframe times of 1.07μs as dictated by the experimental requirements. In principle considerably shorter interframe times are possible. Both MCPIIs and PFDs were used as the shutters for the cameras, both performing satisfactorily, with the PFD gated cameras providing somewhat superior performance overall, but with the added complication of much higher required swings in gating voltage. As with most lens coupled high frame rate camera systems, light intensity was a major issue, with our best camera system limited to slightly less than one photoelectron per proton. The low light levels and high frame rates precluded the use of simpler systems involving beam splitting and light amplification. Future work to improve photoelectron counting statistics will therefore involve the use of faster optics and larger diameter gating devices, thereby larger magnification optical systems which yield more light.

7. REFERENCES

1. N. S. P. King, G. J. Yates, S. A. Jaramillo, J. W. Ogle, and J. L. Detch Jr., "Nanosecond Gating Properties of Proximity-Focused Microchannel-Plate Image Intensifiers," Los Alamos Conference on Optics, SPIE Vol. 288, pp. 426–433, April 7–10, 1981, Santa Fe, New Mexico.

2. G. J. Yates and Nicholas S. P. King, "Measured Responsivities of Generation II and Hybrid Image Intensifiers," SPIE Vol. 2551, Photoelectronic Detectors, Cameras, and Systems, pp. 145–158, July 13–14, 1995, San Diego, California.

3. Bicron Corporation, 12345 Kinsman Road, Newbury, OH 44065.

4. C. Thomas Mottershead and John D. Zumbro, "Magnetic Optics For Proton Radiography," Proceedings of the Particle Accelerator Conference, Vancouver, Canada, May 1997.